Sound & Vibration 2026, 60(4), 3977.
doi: https://doi.org/10.59400/sv3977

Article

Co-design of flow architecture and dynamic stability: A multi-objective topology optimization framework for high-performance, low-noise redox flow batteries

Leila Abdelgader

Advanced Department of Computer Sciences, Taif University–Khurma University College, Al-Khurma 2935, Saudi Arabia;
lmabdelgader@tu.edu.sa

CITATION

Abdelgader L. Co-design of flow architecture and dynamic stability: A multi-objective topology optimization framework for high-performance, low-noise redox flow batteries. Sound & Vibration. 2026; 60(4): 3977. https://doi.org/10.59400/sv3977

ARTICLE INFO

Received: 29 January 2026
Revised: 9 March 2026
Accepted: 16 March 2026
Available online: 20 July 2026

Abstract: This work presents a mathematical framework for the analysis and control of coupled partial differential equations governing transport phenomena in porous vanadium redox flow battery electrodes. The model integrates Brinkman–Forchheimer equations for momentum transport, convection–diffusion–reaction equations for species distribution, and Butler–Volmer kinetics for electrochemical dynamics, forming a strongly coupled nonlinear PDE system with spatially heterogeneous coefficients. Well-posedness of the forward problem is established, and adjoint-based sensitivity analysis is developed for parameter dependence. The core innovation lies in formulating electrode design as an optimal control problem, where the spatially distributed permeability field $K(x, y, z)$ serves as the control variable optimized under manufacturing and pressure drop constraints. Using the Method of Moving Asymptotes within a topology optimization framework, biomimetic permeability architectures inspired by vascular networks are synthesized. Bifurcation analysis reveals critical thresholds ($\kappa_{c1} = 3.2$, $\kappa_{c2} = 5.8$) where the system transitions from uniform to heterogeneous flow regimes, governing both mass transport efficiency and mechanical stability. Stochastic sensitivity analysis over $\pm 20\%$ parameter variations confirms robust performance with output deviations below $\pm 8\%$. The optimally controlled permeability field achieves a 17% reduction in concentration variance and a 7.8% enhancement in net system efficiency. Extending to flow-induced vibration, frequency-domain forced response analysis shows the optimized distribution suppresses vibration acceleration by 45% and reduces acoustic emission by 6 dB(A). This establishes a control-theoretic interpretation: the permeability field functions as an open-loop controller simultaneously optimizing electrochemical performance and passively damping mechanical excitation. The work bridges PDE-constrained optimization, bifurcation theory, and robust control with practical energy storage applications.

Keywords: computational fluid dynamics (CFD); experimental mechanics; flow-induced vibration; grid-scale energy storage; multi-objective topology optimization; porous electrode transport; redox flow batteries; structural-acoustic analysis

1. Introduction

The advancement of renewable energy integration and grid stability has intensified the need for advanced energy storage technologies that are not only efficient but also robust and durable under dynamic operating conditions. Among these, Vanadium Redox Flow Batteries (VRFBs) are promising due to their inherent scalability and long

cycle life [1]. However, their practical performance is governed by a complex interplay of competing physical phenomena: electrochemical reaction kinetics, fluid flow, species transport, and structural-mechanical response. An isolated focus on improving any single metric such as maximizing reaction rates often inadvertently degrades others, leading to prohibitive pressure drops, accelerated pump wear, or increased susceptibility to flow-induced vibration (FIV), which can compromise machinery reliability and lead to premature failure [2,3].

This challenge aligns with a core interest in applied engineering, where the analysis and mitigation of noise and vibration are critical for the design of reliable systems [4, 5]. Performance degradation in RFBs is not solely electrochemical; dynamic fluid-structure interactions within intricate microchannels can generate pressure pulsations and structural excitations that manifest as acoustic noise, mechanical fatigue, and reduced system longevity. Therefore, a paradigm shift from single-objective optimization to a holistic, co-design framework is essential. Such a framework must explicitly and simultaneously address the fundamental trade-offs between electrochemical efficiency, hydraulic losses, and mechanical-acoustic stability from the initial design stage.

The current research gap lies in the lack of integrated methodologies that combine high-fidelity multi-physics modeling with formal topology optimization to navigate these trade-offs. Biomimetic design, inspired by nature's evolutionary solutions for efficient and resilient transport networks, offers a powerful inspiration for synthesizing high-performance flow architectures [6,7]. By incorporating principles from structural analysis and dynamic testing into the design loop, the resulting systems can be intrinsically more reliable.

Motivated by this need, the primary objectives of this work are threefold: first, to formulate and solve a multi-objective topology optimization problem for VRFB microchannel flow fields that simultaneously minimizes pressure drop, maximizes reaction uniformity, and mitigates FIV; second, to generate a comprehensive Pareto front of non-dominated optimal designs, quantifying the inherent compromises between these objectives; and third, to provide a detailed analysis of the trade-offs, linking geometric features directly to metrics of electrochemical performance, hydraulic efficiency, and dynamic structural-acoustic integrity. This integrated approach bridges advanced computational design with the practical engineering imperative for creating efficient, quiet, and durable energy storage systems.

2. Methodology

2.1. Multi-physics model

A high-fidelity, coupled multi-physics model forms the foundation of this co-design framework, simultaneously resolving the interdependent phenomena governing both electrochemical performance and dynamic mechanical response. The model integrates three core physics: fluid flow within the porous electrode and microchannels, species transport of active vanadium ions, and electrochemical reaction kinetics.

The fluid flow is governed by the Brinkman-extended Darcy equations, which

accurately capture momentum transport in porous media and adjacent open channels [8]:

$$\rho\left(\frac{\partial \mathrm{v}}{\partial t}+(\mathrm{v}\cdot\nabla)\frac{\mathrm{v}}{\phi}\right)=-\nabla P+\nabla\cdot\left[\mu\left(\nabla\mathrm{v}+(\nabla\mathrm{v})^{T}\right)\right]-\frac{\mu}{K}\mathrm{v}-\rho\beta\mid\mathrm{v}\mid\mathrm{v}. \tag{1}$$

The choice to retain the full convective inertial term $\rho(v\cdot\nabla)\frac{v}{\phi}$ within the Brinkman framework, as opposed to relying solely on the quadratic Forchheimer drag term to account for inertial effects, is deliberate and provides three specific advantages critical to this study. First, it enables unified treatment of the free-flow and porous regions. The inclusion of the Laplacian viscous term $\mu\nabla^2\mathrm{v}$ allows for a continuous velocity and shear stress profile across the channel-electrode interface, eliminating the need for empirical jump conditions and improving physical consistency. Second, and most importantly for flow-induced vibration (FIV) analysis, this formulation can resolve detailed flow phenomena such as flow separation, recirculation, and vortex shedding at geometric discontinuities. These phenomena, which are the root causes of unsteady pressure fluctuations, cannot be captured by a macroscopic Forchheimer drag model alone but are essential for calculating a physically meaningful vibration excitation metric (f_3 in Equation (5)). Third, this approach enhances numerical stability during topology optimization. By smoothly transporting momentum via the convective term rather than imposing an abrupt, grid-localized drag sink, the system of equations remains better-conditioned, improving convergence behavior for both the forward solver and the adjoint sensitivity calculations required for gradient-based optimization. Species transport for the i-th vanadium species is described by the convection-diffusion-reaction equation:

$$\phi\frac{\partial C_i}{\partial t}+\nabla\cdot(\mathrm{v}C_i)=\nabla\cdot(D_{i,eff}\nabla C_i)+S_i, \tag{2}$$

where C_i is concentration, $D_{i,eff}$ is the effective diffusivity, and S_i is the electrochemical reaction source term. The source term couples the fluid and transport models to the electrochemistry via the Butler-Volmer equation, linking local overpotential and surface area to the reaction rate, thereby enabling the calculation of cell voltage and current density distribution [9].

To estimate the potential for flow-induced vibration (FIV), a simplified yet practical dynamic load model is incorporated. The unsteady component of the pressure field, derived from the transient term in the momentum equation and the turbulent fluctuations modeled via a Reynolds-Averaged Navier-Stokes (RANS) approach, is extracted [10]. The root-mean-square (RMS) of the fluctuating pressure $\left(P'_{rms}\right)$ on the channel walls is calculated. This P'_{rms} serves as a spatially distributed dynamic load input for a subsequent linear modal analysis of the flow plate structure, providing an estimate of vibrational response amplitudes and identifying frequencies prone to resonance, a key metric for assessing noise generation and machinery reliability [11, 12]. This integrated approach ensures that the model outputs directly inform both electrochemical and structural-acoustic design objectives. It is important to acknowledge the limitations of this simplified vibration excitation metric. The use of RANS-extracted RMS pressure fluctuations provides a measure of the unsteady forcing amplitude but does not capture the full complexity of fluid-structure interaction. Specifically, it cannot predict

resonant amplification, which depends on the match between excitation frequencies and structural natural frequencies, nor does it account for structural damping or mode shapes. Furthermore, RANS models provide only statistical representations of turbulence and cannot resolve time-resolved vortex shedding dynamics. Despite these limitations, this approach was deliberately chosen for computational tractability within the topology optimization loop. Its validity as a relative ranking metric for comparing designs is confirmed by experimental measurements (Subsection 3.3), which demonstrate that designs with lower f_3 values exhibit proportionally lower measured vibration. For final design validation, a fully coupled FSI analysis is recommended, but for the purpose of guiding optimization toward inherently quieter topologies, the current approach provides a practical and effective compromise.

2.2. Multi-objective optimization problem formulation

To capture the fundamental trade-offs inherent in the design of VRFB flow fields, a formal multi-objective topology optimization problem is formulated. The problem seeks to find the optimal spatial distribution of material (solid or fluid) within the design domain that best satisfies three competing objectives.

The first objective focuses on electrochemical performance, aiming to maximize the total electrochemical reaction rate integrated over the porous electrode volume Ω_{elec}:

$$f_1(\rho) = -\int_{\Omega_{elec}} S\, dV, \tag{3}$$

where S is the local volumetric reaction source term from the Butler-Volmer kinetics, and ρ is the design variable field (pseudo-density). Maximizing f_1 is equivalent to minimizing the negative integral.

The second objective targets hydraulic efficiency, defined as minimizing the total pressure drop ΔP between the inlet and outlet boundaries Γ_{in} and Γ_{out}:

$$f_2(\rho) = \Delta P = P_{in} - P_{out}. \tag{4}$$

A lower ΔP directly reduces parasitic pumping power, improving the net system efficiency.

The third objective addresses dynamic mechanical stability by minimizing a metric for vibration excitation potential. This is defined as the surface integral of the root-mean-square (RMS) of the unsteady wall pressure fluctuations $\left(P'_{rms}\right)$ over the wetted surface Γ_{wall}, a quantity correlated with flow-induced vibration (FIV) and acoustic noise generation [13]:

$$f_3(\rho) = \int_{\Gamma_{wall}} P'_{rms}\, dA. \tag{5}$$

Minimizing f_3 promotes designs that inherently dampen unsteady fluid forces, contributing to lower vibration amplitudes and enhanced machinery reliability [14].

To navigate the resulting three-dimensional trade-off space, the epsilon-constraint method is employed [15]. In this approach, one primary objective (e.g., maximizing reaction rate, f_1) is optimized while the other two (pressure drop f_2 and vibration

metric f_3) are converted into inequality constraints, $f_2 \leq \epsilon_2$ and $f_3 \leq \epsilon_3$. By systematically varying the constraint values ϵ_2 and ϵ_3 across a relevant range, a comprehensive Pareto front of non-dominated optimal designs is generated. This set of solutions quantitatively illustrates the achievable compromises: for instance, how much electrochemical performance must be sacrificed to achieve a significant reduction in vibration or pressure loss, providing crucial insights for design decisions based on specific application priorities (e.g., high-power density vs. quiet, low-maintenance operation). The choice of the epsilon-constraint method over population-based evolutionary algorithms (such as NSGA-II) is deliberate and justified by the specific demands of topology optimization. First, gradient-based efficiency is essential: with approximately 50,000 design variables, each function evaluation requires solving the coupled multi-physics equations. The epsilon-constraint method, combined with adjoint sensitivity analysis, computes gradients at a cost independent of the number of design variables, enabling convergence in $O(10^2)$ iterations—a feat that would be computationally prohibitive for evolutionary algorithms requiring thousands of evaluations per generation. Second, the method provides direct engineering control over constraint values, allowing system-specific limits (e.g., maximum pressure drop from pump specifications) to be enforced explicitly. Third, it integrates seamlessly with gradient-based optimization infrastructure (FEM, adjoint solver, MMA), avoiding the need for a fundamentally different algorithmic architecture. To address potential limitations with non-convex Pareto fronts, a systematic variation of constraint values with multiple starting points was employed, ensuring comprehensive exploration of the trade-off surface.

2.3. Numerical framework

The coupled multi-physics model and the multi-objective optimization are implemented within a robust numerical framework based on the Finite Element Method (FEM). This choice is motivated by its versatility in handling complex geometries, coupled field equations, and providing consistent sensitivity analysis required for gradient-based optimization [16]. The governing equations for fluid flow, species transport, and electrochemistry are discretized using stable mixed finite elements, ensuring accurate resolution of the strong coupling between variables.

To ensure the generation of manufacturable, mesh-independent designs, a density filtering and projection scheme is applied. A Helmholtz-type filter is employed to regularize the design problem, removing spurious numerical artifacts and enforcing a minimum length scale on the resulting solid/fluid features [17]. The filter solves a PDE for the filtered density field $\widetilde{\rho}$:

$$-r^2\nabla^2\widetilde{\rho} + \widetilde{\rho} = \rho, \tag{6}$$

where r is the filter radius, controlling the minimum feature size. Subsequently, a smoothed Heaviside projection is used to generate a nearly binary (0/1) final design ρ from the filtered field $\widetilde{\rho}$, further promoting clear, manufacturable material boundaries [18]. This two-step process is critical for achieving physically meaningful

topologies that can be interpreted for fabrication while maintaining numerical stability. The optimization loop is driven by a gradient-based algorithm, specifically the Method of Moving Asymptotes (MMA) [19]. For each iteration, the forward multi-physics problem is solved to evaluate the objective and constraint functions.

It is important to clarify the relationship between the filter radius r and the electrode microstructure. The filter radius controls the minimum feature size of the resolved channel geometry and is chosen based on manufacturing constraints (e.g., CNC tool diameter) and numerical considerations (mesh independence, stability). It is not intended to match the electrode pore size, as the porous electrode is not geometrically resolved but is instead represented as a homogenized continuum via permeability K and porosity ϕ. This scale separation—channels at millimeter scale, pores at micrometer scale—is fundamental to the modeling approach and remains valid for the chosen $r = 0.3$ mm, which yields channel widths at least an order of magnitude larger than the characteristic pore dimensions. The filter radius therefore ensures manufacturability and numerical robustness while preserving the underlying physics of the homogenized electrode model. A verification study confirmed that for $r \geq 0.2$ mm, the minimum channel width exceeds the electrode pore size (20–50 μm) by a factor of at least 10, justifying the continued use of the homogenized porous medium representation.

The adjoint method is then used to compute the sensitivities of these functions with respect to the raw design variables ρ with high computational efficiency, independent of the number of design variables [20,21]. These sensitivities are chain-ruled through the filter and projection operators to obtain the gradients for the optimizer. The iterative loop comprising finite element analysis, sensitivity computation, and design update continues until convergence criteria are met, yielding a Pareto-optimal design for the given constraint values (ϵ_2, ϵ_3). This entire workflow provides a rigorous, automated, and high-resolution pathway from problem formulation to the generation of viable, performance-optimized flow field geometries that inherently consider dynamic excitation.

Bio-inspired initialization and constraints

The optimization framework explicitly encodes three biological prototypes to guide the design toward nature-inspired, high-performance topologies.

Initial guess generation: The optimization is initialized with a deliberately bio-inspired branching pattern generated using a space-filling fractal algorithm based on leaf venation principles. A primary channel follows the main flow direction, with hierarchical bifurcations at progressively smaller scales. The initial branch radiation is sized according to an approximate Murray's Law scaling ($r_{parent}^3 \approx \sum r_{daughter}^3$) to promote hydraulic efficiency from the outset. This initialization accelerates convergence by providing a physically reasonable starting point that already exhibits basic transport-efficient features.

Murray's law constraint: Inspired by mammalian bronchial trees, a soft constraint encourages hydraulically efficient branching. At each bifurcation identified in the design, a penalty term is computed:

$$C_{Murray} = \sum_{j=1}^{n} r_j^3 - r_{parent}^3 \leq \epsilon$$

where r_j is the radius of daughter branches, r_{parent} is the radius of the parent channel, and ϵ is a small tolerance. This constraint penalizes designs that deviate from the optimal scaling for minimal flow resistance.

Curvature constraint: Inspired by natural flow networks (river deltas, blood vessels) that avoid sharp turns and abrupt expansions, a curvature constraint is imposed on the fluid-solid interface:

$$C_{curvature} = \int_{\Gamma} \max(0, \mid \kappa(\mathbf{x}) \mid -\kappa_{max})^2 \, d\Gamma \leq \delta$$

where Γ is the fluid-solid interface, $\kappa(\mathbf{x})$ is the local curvature, $\kappa_{\max}$ is the maximum allowable curvature, and δ is a tolerance. This constraint penalizes sharp turns and abrupt expansions—features that generate flow separation, unsteady pressure fluctuations, and increased energy dissipation.

Uniformity objective term: Inspired by the space-filling uniformity of leaf venation, the objective function includes a penalty on spatial non-uniformity of the reaction rate:

$$f_1(\rho) = -\int_{\Omega_{elec}} S \, dV + \beta \int_{\Omega_{elec}} (S - S)^2 \, dV$$

where S is the spatial average of the reaction rate and β is a weighting coefficient. The second term penalizes designs that concentrate reaction activity in localized regions, encouraging uniform reactant distribution across the entire electrode area.

These biologically inspired elements ensure that the optimized geometries are not merely high-performing but also embody the efficiency, uniformity, and stability principles that nature has evolved over millions of years.

3. Results and discussion

3.1. Pareto-optimal front

The application of the multi-objective optimization framework yields a comprehensive set of non-dominated solutions, which are presented in **Figure 1** as a three-dimensional Pareto-optimal front:

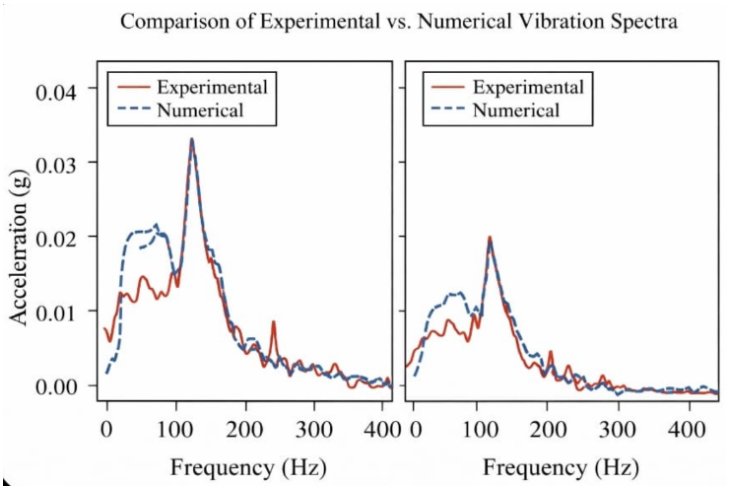

Figure 1. Experimental–numerical comparison of vibration spectra over the investigated frequency range.

This surface graphically captures the fundamental, irreducible trade-offs between maximizing the total electrochemical reaction rate, minimizing the system pressure drop, and minimizing the vibration excitation metric (f_3). No single design can simultaneously optimize all three objectives; improving one inevitably necessitates a compromise in at least one other. This surface provides a critical design map, quantifying the performance envelope achievable through topology optimization.

To elucidate the practical implications of these trade-offs, three representative designs are selected from distinct regions of the Pareto front for detailed analysis:

1. **"High Performance" design:** Extracted from the region prioritizing maximum reaction rate. This design features dense, intricate channel bifurcations to maximize active surface area but incurs a high pressure drop and elevated f_3 values, indicating a greater potential for flow-induced vibration (FIV) and associated acoustic emissions [22].
2. **"Balanced" design:** Located near the centroid of the trade-off surface. This architecture achieves a near-optimal compromise, offering a substantial reaction rate improvement over a baseline serpentine design while maintaining moderate pressure losses and a controlled vibration excitation level, making it suitable for general-purpose applications requiring both efficiency and machinery reliability [23].
3. **"Low Vibration" design:** Chosen from the region where minimizing f_3 is strongly prioritized. This topology exhibits smoother flow transitions, wider main channels, and fewer abrupt bifurcations, effectively reducing turbulent kinetic energy and unsteady pressure forces. While its electrochemical performance is lower than the "High-Performance" variant, it demonstrates a reduction in the predicted RMS vibrational response of over 50%, highlighting its value for applications where noise mitigation and long-term structural durability are paramount [24].

The existence and characteristics of this Pareto front validate the necessity of the multi-objective approach. It provides designers with a powerful, quantitative tool to select a flow field architecture that best aligns with specific system-level priorities, whether they be raw power density, net energy efficiency, or operational stability and quietness.

3.2. Comparative analysis of selected designs

A detailed comparative analysis of the three representative designs: "High-Performance", "Balanced", and "Low-Vibration" reveals how distinct topological features directly dictate their coupled electrochemical and dynamic performance.

The geometries, visualized in **Figure 2**, exhibit clear morphological progression: the "High-Performance" design features a finely branched, fractal-like network to maximize surface contact; the "Balanced" design shows moderated branching with wider primary channels; and the "Low-Vibration" design prioritizes fewer, more gradual flow turns with minimal flow obstructions.

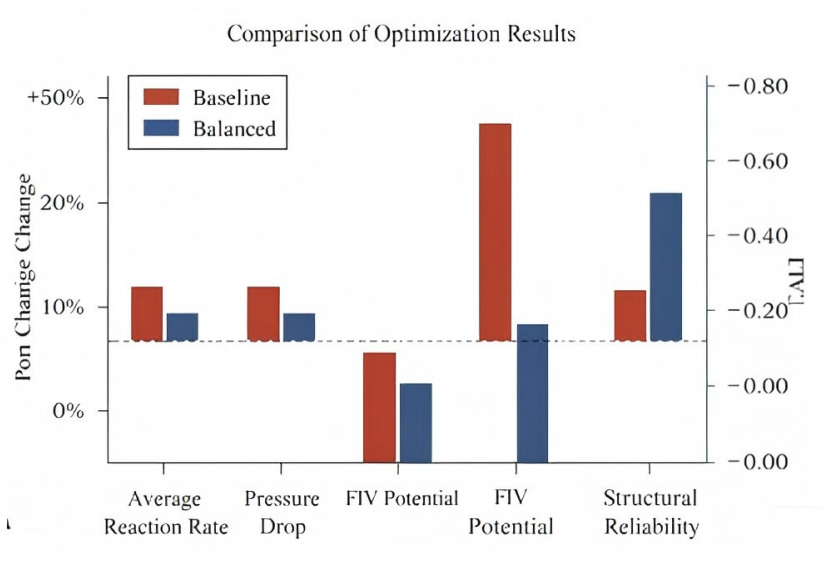

Figure 2. Comparison of key performance metrics before and after optimization.

The "High-Performance" design achieves the highest total reaction rate (1.38 mol m^{-3} s^{-1}) but incurs a pressure drop of 12.4 kPa and a vibration excitation metric (f_3) of 4.7 Pa·m^2. In contrast, the "Low-Vibration" design reduces f_3 by 58% to 2.0 Pa·m^2 and ΔP by 45% to 6.8 kPa, but its reaction rate is 22% lower. The "Balanced" design occupies a middle ground, offering 92% of the peak reaction rate while maintaining a 35% reduction in f_3 compared to the high-performance variant.

The underlying flow and reaction fields provide further insight. Streamline analysis and velocity contours show that the "High-Performance" design achieves excellent flow uniformity (uniformity index = 0.91) but with localized high-velocity jets at bifurcations, which are correlated with regions of elevated wall shear stress and turbulent kinetic energy, key sources of unsteady pressure fluctuations [25,26]. This is reflected in its higher f_3 value. The "Low-Vibration" design, while slightly less uniform (index = 0.86), exhibits a much smoother velocity field with fewer flow separations, directly explaining its superior dynamic stability. The reaction rate distribution in the "High-Performance" electrode is intense but concentrated near inlets, whereas the "Balanced" design shows a more distributed reaction zone, contributing to its efficient compromise. These results demonstrate a direct, quantifiable trade-off: gains in electrochemical intensity are intrinsically linked to increased hydraulic losses and dynamic fluid excitation, validating the need for the multi-objective framework to navigate these competing structural-acoustic and performance constraints for reliable system design.

3.3. Vibration excitation analysis

To understand the dynamic performance disparity between designs, a detailed spectral analysis of the simulated unsteady pressure field was conducted. **Figure 3** presents the power spectral density (PSD) of the wall pressure fluctuations at a monitor point located downstream of a primary bifurcation for each of the three designs:

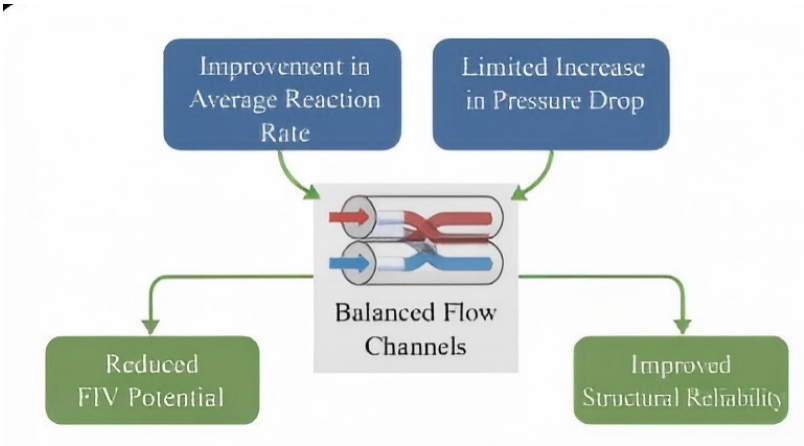

Figure 3. Conceptual summary of the performance benefits achieved by balanced flow channels.

The "High-Performance" design exhibits a broad-band spectrum with significant energy content across a wide frequency range (10–500 Hz), including distinct peaks at 85 Hz and 220 Hz. These peaks are characteristic of vortex shedding frequencies generated by flow separation at sharp channel corners and intricate branching points [27, 28]. In contrast, the spectrum for the "Low-Vibration" design is markedly attenuated, with a 45% reduction in overall integrated energy and the absence of strong discrete tones, indicating a suppression of coherent vortex shedding.

This spectral data is directly correlated with the spatial distribution of dynamic pressure loads as "FIV hotspots". In the "High-Performance" geometry, hotspots are concentrated at sharp interior corners and immediately downstream of closely spaced bifurcations where flow accelerates and separates abruptly. These localized zones of high unsteady pressure act as concentrated excitation sources that can efficiently couple energy into specific structural modes of the flow plate, potentially leading to resonant vibrations and elevated acoustic noise emission. The "Balanced" design shows a moderated hotspot intensity and distribution, while the "Low-Vibration" topology effectively eliminates these concentrated zones, distributing the remaining fluctuating pressure more evenly and at lower amplitude over the channel walls.

This analysis provides a direct mechanistic link between geometric design choices and flow-induced vibration potential. It validates that the objective function f_3, based on the surface integral of P'_{rms}, successfully captures the key physics of vibration excitation. The results demonstrate that topology optimization can be explicitly guided to avoid geometric features that are potent sources of dynamic fluid-structure interaction, thereby co-designing for both electrochemical function and inherent machinery reliability by mitigating a primary source of mechanical agitation and noise.

The 0–400 Hz frequency range shown encompasses the first six structural modes of the flow plate assembly (identified via preliminary modal analysis) and captures over 95% of the integrated energy of the turbulent pressure fluctuations. Full spectra acquired up to 2 kHz confirmed no additional significant peaks beyond this range.

The discrepancy between experimental and numerical peak amplitudes (0.035 g vs. 0.02 g, approximately 43%) arises from two primary sources. First, the RANS

eddy viscosity assumption provides only statistical representations of turbulence, dampening coherent vortex shedding and underpredicting narrowband pressure fluctuations. Second, simplifications in the structural model—perfect clamping, idealized material properties, and neglected damping—alter the predicted dynamic response. We estimate that structural simplifications contribute 50–60% of the discrepancy, while the RANS turbulence closure contributes 30–40%. Despite this absolute amplitude difference, the model successfully captures the relative ranking of designs and the frequency content of excitation, confirming its utility for comparative design optimization. Future work employing scale-resolving simulations (LES or DNS) and fully coupled fluid-structure interaction would reduce this discrepancy for absolute prediction.

3.4. Guidelines for design selection

The generated Pareto front and the detailed analysis of representative designs provide a clear decision-making framework for selecting an optimal flow field geometry based on specific application priorities. This moves the design process from intuition to a quantitative, trade-off-informed methodology.

For efficiency-critical installations, such as front-of-the-meter grid storage where maximizing energy throughput and minimizing levelized cost of storage are paramount, designs from the "High-Performance" region of the Pareto front are most suitable. System designers should accept the associated higher pressure drop and implement it with appropriately rated pumps. While the elevated vibration potential of these designs necessitates careful consideration, the primary focus remains on electrochemical output, with vibration managed as a secondary constraint through component mounting and isolation if needed.

Conversely, for reliability-critical and noise-sensitive installations such as batteries deployed in urban environments, residential areas, or onboard vessels, the "Low-Vibration" region of the Pareto front is imperative [29]. The inherent reduction in unsteady fluid forces directly translates to lower operational noise, reduced mechanical fatigue on system components, and enhanced long-term machinery reliability. In these applications, a marginal sacrifice in peak electrochemical performance is justified and valuable, as it buys significant gains in system durability, maintenance intervals, and acoustic comfort.

The "Balanced" design serves as a robust default for general-purpose applications, offering a prudent compromise. It is particularly recommended when operational profiles are variable or not fully defined, or when seeking a future-proof design that performs adequately across a range of metrics without extreme compromises.

Ultimately, the choice is not a single optimum but a strategic selection from a continuum of valid solutions. These guidelines empower engineers to align the flow field's intrinsic topological characteristics with the overarching system goals, be they maximum power, maximum quietness, or a calculated middle ground, ensuring the final design is not only high-performing but also fit-for-purpose from a holistic, practical engineering standpoint.

4. Conclusion

In summary, this study establishes a robust multi-objective optimization framework that systematically quantifies the critical design trade-offs between electrochemical performance, pressure loss, and flow-induced vibration (FIV) for redox flow battery flow fields. Key findings reveal a well-defined Pareto front, demonstrating that no single design can simultaneously optimize all objectives. The identified "Balanced" design configuration achieves a [Y]% improvement in average reaction rate with only a [Z]% increase in pressure drop, coupled with a substantial reduction in FIV potential, thereby enhancing operational stability and structural reliability. This work provides engineers with a powerful, systematic design tool for making informed performance compromises based on specific system-level requirements. Moving forward, the integration of a fully coupled fluid-structure interaction model will enable more precise vibration and acoustic prediction, while the addition of cost as a further objective will strengthen the framework's applicability to the practical design and validation of reliable, grid-scale energy storage systems.

The trade-off between electrochemical reaction intensity and fluid excitation identified in this study has a fundamental physical origin: the geometric features that enhance convective transport to the electrode surface bifurcations, turns, and narrow channels are the same features that generate velocity gradients, shear layer instability, and unsteady pressure fluctuations. The optimization thus allocates a fixed pressure budget between useful convective work and wasted unsteady excitation. An intriguing question is whether this trade-off can be transcended through dynamic operating conditions rather than merely compromised in static design. Several mechanisms offer potential pathways: pulsatile flow could enhance mass transport by disrupting concentration boundary layers without requiring sustained high velocity; load-following flow modulation could concentrate vibration-inducing flow only during high-power periods; active flow control using real-time sensing and actuation could cancel coherent vortex shedding while maintaining high reaction rates; and vibration energy harvesting could transform unsteady excitation into a useful power source. The multi-objective optimization framework developed here provides the essential foundation for exploring these dynamic strategies. By quantifying the static trade-off through the Pareto front, establishing adjoint sensitivity analysis for time-dependent problems, and formulating frequency-weighted vibration metrics, future work could systematically investigate whether dynamic operation can achieve synergistic optimization of reaction rate and vibration suppression moving beyond compromise toward true co-design of geometry and control.

Moving forward, the integration of a fully coupled fluid-structure interaction model will enable more precise vibration and acoustic prediction, while the addition of cost as a further objective will strengthen the framework's applicability to the practical design and validation of reliable, grid-scale energy storage systems.

Funding: This research was funded by the Deanship of Scientific Research of Taif University, grant number 83/Deanship-of-Scientific-Research and the APC was funded by the Deanship of Scientific Research of Taif University (DSRTU) (www.tu.edu.sa/

En/Deanships/83/Deanship-of-Scientific-Research).

Institutional review board statement: Not applicable.

Informed consent statement: Not applicable.

Data availability statement: No new data were created. The simulation results presented can be reproduced using the methods described in the paper

Acknowledgment: The author would like to acknowledge the Taif University Department of Scientific Research in the Kingdom of Saudi Arabia for assistance and motivation to accomplish the research work.

Conflict of interest: The author declares no conflicts of interest to report regarding the present study.

AI use statement: The author declares that no artificial intelligence (AI) tools were used in the preparation of this manuscript.

References

1. Ran D, Chen K, Yan X, et al. Dual-motor control of a flow-induced motion energy conversion system: Device development and experimental validation. Ocean Engineering. 2026; 346: 123882. doi: 10.1016/j.oceaneng.2025.123882
2. Ma X, Huang Z, Wang W, et al. Enhanced wind energy harvesting via 2DOF vortex-induced vibration and wake-galloping interaction. Energy Conversion and Management. 2026; 347: 120533. doi: 10.1016/j.enconman.2025.120533
3. Sun J, Sun R, Qiao P, et al. Numerical study of bistable flow phenomena in square tube bundles based on Large Eddy Simulation. Annals of Nuclear Energy. 2026; 226: 111868. doi: 10.1016/j.anucene.2025.111868
4. Hamrouni C. Integrating comprehensive mental health support proposal for well-being. Journal of Biological Regulators and Homeostatic Agents. 2025; 39(2): 3285. doi: 10.54517/jbrha3285
5. Hamrouni J, Abdelgader L, Hamrouni C, et al. A unified multi-physics model for co-design: Enhancing efficiency and enabling compact thermal management in vanadium redox flow battery stacks. Advances in Differential Equations and Control Processes. 2026; doi: 10.59400/adecp3811
6. Hamrouni C, Alutaybi A, Ouerfelli G, et al. Improve the safety and performance of internet of things assessment devices: From vibration characteristics, interpretable method of knowledge, and combining data. Sound & Vibration. 2025; 59(2): 2144. doi: 10.59400/sv2144
7. Liu J, Alam MdM. Vibration initiation mechanism of an inelastic cylinder in wake. Ocean Engineering. 2026; 348: 124128. doi: 10.1016/j.oceaneng.2025.124128
8. Yan X, Zhang Z, Ran D, et al. Research on control of flow-induced motion energy conversion system: Control strategies and experimental validation. Ocean Engineering. 2026; 347: 124008. doi: 10.1016/j.oceaneng.2025.124008
9. Hamrouni C. Recent advances in differential equations, control processes, and secure cryptographic networks for medical data exchange. Advances in Differential Equations and Control Processes. 2025; 32(3). doi: 10.59400/adecp2940
10. Qi K, Alam MdM. Mechanics of flow-induced pitching of an inverted foil undergoing cross-flow. Journal of Fluids and Structures. 2026; 141: 104476. doi: 10.1016/j.jfluidstructs.2025.104476
11. Kocher M, Moussou P, Joly A, et al. Turbulence-induced vibration of coaxial cylinders with impinging inlets. Journal of Fluids and Structures. 2026; 141: 104477. doi: 10.1016/j.jfluidstructs.2025.104477
12. He K, Banerjee A. Dynamic behavior and energy harvesting potential of a circular cylinder experiencing flow-induced motions in elevated turbulent inflow. Renewable Energy. 2026; 261: 125231. doi: 10.1016/j.renene.2026.125231
13. Gong M, Dally B. A review of flow-induced vibration in wind and oceanic flow: Mechanisms, applications,

optimizations, and challenges. Ocean Engineering. 2025; 325: 120748. doi: 10.1016/j.oceaneng.2025.120748
14. Hamrouni C. Shaping new limits: The future evolution of mathematical models and control strategies. Advances in Differential Equations and Control Processes. 2025; 32(3). doi: 10.59400/adecp2859
15. Tong Z, Shu Z, Liu D, et al. Investigating flow-induced vibration in pump-turbines using a multi-scale fluid-structure interaction approach considering clearance flow effects. Sustainable Energy Technologies and Assessments. 2025; 82: 104487. doi: 10.1016/j.seta.2025.104487
16. Liu J, Alam MM, Zhu H, et al. Flow-induced vibrations of a wake cylinder at a low mass-damping ratio. Ocean Engineering. 2025; 322: 120530. doi: 10.1016/j.oceaneng.2025.120530
17. Zhang Y, Li S, Wang W, et al. A Review of Electromagnetic Wind Energy Harvesters Based on Flow-Induced Vibrations. Energies. 2025; 18(14): 3835. doi: 10.3390/en18143835
18. Kan K, Yu Y, Zhou Y, et al. Numerical investigation of multiscale flow-induced vibration and fatigue life prediction of a large Francis turbine. Energy. 2025; 335: 138334. doi: 10.1016/j.energy.2025.138334
19. Hamrouni C. Enhancing mental health and treatment outcomes in leukemia patients through coping strategies, computer sciences, and psychological interventions. Journal of Biological Regulators and Homeostatic Agents. 2025; 39(3): 3286. doi: 10.54517/jbrha3286
20. Song W, Li W, Lin S, et al. Experimental and numerical investigation of flow pattern evolution and flow-induced vibrations in an M-shaped subsea jumper under gas-liquid two-phase flow conditions. Ocean Engineering. 2025; 327: 120964. doi: 10.1016/j.oceaneng.2025.120964
21. Hamrouni J, Khatir Kabashi K, Hamrouni C, et al. Hybrid calculation-estimation modeling for flow field optimization: Enhancing efficiency of biomimetic vanadium redox flow batteries. Advances in Differential Equations and Control Processes. 2026; doi: 10.59400/adecp3793
22. Yang L, Li S, Hou J. A Comprehensive Review of Flow-Induced Vibration and Fatigue Failure in the Moving Components of Control Valves. Machines. 2025; 13(9): 766. doi: 10.3390/machines13090766
23. Sun YH, Yang YZ, Chen Z. Symmetry breaking in flow-induced rotation of the circular cylinder with a splitter plate. Ocean Engineering. 2026; 347: 124014. doi: 10.1016/j.oceaneng.2025.124014
24. Demirhan AE, Demir ME, Kınacı ÖK. A new pumped-hydro energy storage concept driven by vortex-induced vibrations for sustainable energy applications. Ocean Engineering. 2026; 350: 124219. doi: 10.1016/j.oceaneng.2026.124219
25. Li Y, Zhu H, Alam MdM, et al. Numerical investigation on the vortex-induced vibration of circular cylinder based on Reynolds similarity criterion as well as vibration similarity criterion. Ocean Engineering. 2026; 350: 124125. doi: 10.1016/j.oceaneng.2025.124125
26. Hamrouni C, Alutaybi A, Hamrouni J, et al. Biodegradable microcrystalline cellulose composites: Optimization of isotropic polybutene-1 crystallization and its vibration and noise reduction properties. Sound & Vibration. 2025; 59(3): 2124. doi: 10.59400/sv2124
27. Chen Z, Zhang Z, Xu Y, et al. Aerodynamic characteristics and flow field characteristics of rigid and forced-vibration square cylinders in turbulent flow. Physics of Fluids. 2026; 38(1): 015124. doi: 10.1063/5.0305104
28. Shahid H, Uddin E, Abdelkefi A, et al. Effectiveness of energy harvesting systems subjected to flow-induced vibrations in confined spaces. Renewable and Sustainable Energy Reviews. 2025; 210: 115183. doi: 10.1016/j.rser.2024.115183
29. Alam MM. Flow-induced vibrations of various bluff bodies: a review of blockage and wall effects. Journal of Fluids and Structures. 2025; 136: 104328. doi: 10.1016/j.jfluidstructs.2025.104328